

# Measuring the X-shaped structures in edge-on galaxies

S. S. Savchenko,<sup>1\*</sup> N. Ya. Sotnikova,<sup>1</sup> A. V. Mosenkov,<sup>1,2</sup> V. P. Reshetnikov<sup>1</sup>  
and D. V. Bizyaev<sup>3,4</sup>

<sup>1</sup>*St. Petersburg State University, 7/9 Universitetskaya nab., St. Petersburg, 199034 Russia*

<sup>2</sup>*Sterrenkundig Observatorium, Universiteit Gent, Krijgslaan 281 S9, B-9000 Gent, Belgium*

<sup>3</sup>*Apache Point Observatory and New Mexico State University, Sunspot, NM, 88349, USA*

<sup>4</sup>*Sternberg Astronomical Institute, Moscow State University, Moscow, Russia*

Accepted 2017 July 13. Received 2017 July 6; in original form 2017 April 7

## ABSTRACT

We present a detailed photometric study of a sample of 22 edge-on galaxies with clearly visible X-shaped structures. We propose a novel method to derive geometrical parameters of these features, along with the parameters of their host galaxies based on the multi-component photometric decomposition of galactic images. To include the X-shaped structure into our photometric model, we use the IMFIT package, in which we implement a new component describing the X-shaped structure. This method is applied for a sample of galaxies with available SDSS and *Spitzer* IRAC 3.6  $\mu\text{m}$  observations. In order to explain our results, we perform realistic  $N$ -body simulations of a Milky Way-type galaxy and compare the observed and the model X-shaped structures. Our main conclusions are as follows: (1) galaxies with strong X-shaped structures reside in approximately the same local environments as field galaxies; (2) the characteristic size of the X-shaped structures is about 2/3 of the bar size; (3) there is a correlation between the X-shaped structure size and its observed flatness: the larger structures are more flattened; (4) our  $N$ -body simulations qualitatively confirm the observational results and support the bar-driven scenario for the X-shaped structure formation.

**Key words:** galaxies: spiral – techniques: photometric – methods: data analysis

## 1 INTRODUCTION

Galaxies with boxy/peanut-shaped (B/PS) bulges were found as a curious deviation from normal galaxies with spherical-shaped bulges by Burbidge & Burbidge (1959). It is known now that the B/PS features are rather common in galaxies: the modern estimations of their probability vary from 20% (Yoshino & Yamauchi 2015) up to 40–45% (Lütticke et al. 2000; Laurikainen & Salo 2016) among all disc galaxies observed edge-on. Erwin & Debattista (2017) found that the frequency of these features in disc galaxies strongly depends on the galaxy mass and Hubble type: the B/PS fraction is higher in massive S0–Sa galaxies than in the other types.

As Bureau et al. (2006) found for a sample of 30 edge-on galaxies observed in the  $K$ -band, the galaxies with a B/PS bulge tend to have a more complex morphology than galaxies with other bulge types. These galaxies harbour the centered or off-centered X-shaped structures, secondary maxima of brightness along the major-axis, and spiral-like structures. Their surface brightness profiles are also more complex than in the galaxies with classical bulges: usually they have breaks in their profiles (Freeman Type II profiles, Freeman 1970).

Infrared observations and photometry of the red clump stars in the Galactic bulge revealed that our Galaxy also contains a central X-shaped structure (Laurikainen et al. 2014; Nataf et al. 2015; Ness & Lang 2016). In the recent work by Ciambur & Graham (2016) the first attempt to quantify the properties of B/PS-structures is made. They used the Fourier analysis to describe the surface brightness distribution in the central regions of galaxies and retrieved some parameters of the X-shaped structures, such as their sizes both in radial and vertical directions with respect to the galactic midplane, the integrated ‘strength’, and the peak amplitude of the  $B_6$  Fourier component.

A commonly accepted model of a B/PS feature formation is the buckling instability of a galactic bar (Pfenniger & Friedli 1991; Athanassoula & Misiriotis 2002). The initially flat bar buckles via the vertical resonance of stellar orbits and becomes thicker. The final observed X-shaped structure is made with a set of these resonance orbits (Combes et al. 1990). This scenario was first obtained in the  $N$ -body simulations by Combes & Sanders (1981), who found that the B/PS-bulges were formed shortly after the bar formation. Patsis, Skokos & Athanassoula (2002) studied the formation of the X-shaped structures from the point of view of individual orbits and found a set of orbit families, a combination of which appears to be X-shaped when viewed edge-on. The evolution of the bar vertical shape including the development of the X-shaped

\* E-mail: s.s.savchenko@spbu.ru

appearance as a result of a recurrent buckling, is demonstrated in [Martinez-Valpuesta, Shlosman & Heller \(2006\)](#).

Observational evidence of the relationship between X-shaped structures and bars was provided by [Bureau & Freeman \(1999\)](#), where the position-velocity diagrams were used to show that almost all edge-on galaxies with the B/PS inner isophotes also host a thick bar. These findings were confirmed by [Chung & Bureau \(2004\)](#), who considered 24 edge-on galaxies with X-shaped structures, and demonstrated that 22 of them show clear kinematic bar signatures. Kinematic identification of X-shaped structures for face-on galaxies was performed in [Méndez-Abreu et al. \(2008\)](#).

Another argument for the bar driven scenario of X-shaped structures is cylindrical rotation ( $\partial v/\partial |z| \sim 0$ ) inside of these features ([Combes et al. 1990](#)). While it is usually the case, [Williams et al. \(2011\)](#) have found a counterexample in their study of five edge-on galaxies: the galaxy IC 4767 does not rotate cylindrically, though it has peanut-shaped central isophotes. The dark halo with the reduced central concentration is required to explain these observations ([Athanasoula & Misiriotis 2002](#)).

Another prominent morphological feature in the central regions of many disc galaxies is a barlense ([Laurikainen et al. 2011](#)). The barlenses and X-shaped structures are considered to be physically the same phenomenon ([Laurikainen & Salo 2017](#)). They have very similar colours, and both features are thick in the comparison with the thin bar ([Herrera-Endoqui et al. 2017](#)), which suggests that these structures are results of the bar secular evolution. The appearance of these structures depends on the galaxy orientation, central flux concentration, and the steepness of the rotation curve in the central regions ([Laurikainen & Salo 2017](#); [Salo & Laurikainen 2017](#)).

Although historically these structures are called B/PS-bulges, the formation mechanism described above suggests that they have little in common with bulges. In this regard, following [Patsis, Skokos & Athanasoula \(2002\)](#), we avoid using the word “bulges” and refer to them as the “X-shaped structures” (or just “X-structures”) instead.

The vertical structure of these features is more profound if a galaxy is seen at the edge-on orientation. However, even in this case an automated retrieval of the parameters of X-shaped structures is a challenging task because the light from the bulge and the disc dominate in the central regions of the galaxy. One approach to solve this problem is to enhance the appearance of the X-shaped structure by some image processing techniques (e.g. using the unsharp masking algorithm presented by [Bureau et al. 2006](#)).

In this work we propose a new approach to the estimation of the X-structure parameters. We describe an algorithm which allows us to derive geometrical parameters of the X-structure, along with the parameters of their host galaxies, via a photometric decomposition procedure. This allows us to separate the light of the X-structure from the light of the host galaxy. Once the model image of the host galaxy is obtained, it can be then subtracted from the galaxy image, leaving the X-structure clearly visible.

To interpret the results of our method, we perform the  $N$ -body simulations of a disc galaxy, in which we clearly observe the emergence of an X-structure. Then we compare the observed X-structure parameters with those obtained in our  $N$ -body simulations.

The structure of the paper is organized as follows. In Sect. 2, we describe our sample of galaxies with visible X-structures. In Sect. 3, we outline the algorithm which we apply for the selected sample. The results of our investigation are shown in Sect. 4. In Sect. 5, we describe the method of constructing our  $N$ -body mod-

els that produce the X-structures, and analyze the obtained results. General conclusions are given in Sect. 6.

## 2 THE SAMPLE

Our sample of galaxies with the X-shaped structures is drawn from the EGIS catalogue ([Bizyaev et al. 2014](#)), which contains 5747 edge-on galaxies. To form the sample of galaxies with prominent X-structures, we visually inspected SDSS<sup>1</sup> images of the EGIS galaxies. We considered all (2021) galaxies with diameter estimated within the limits at the level of signal-to-noise of 2 per pixel in the  $r$  band larger than 1 arcmin, and selected galaxies with noticeable central X shapes. Only the galaxies with X-shaped structures are included in our sample. Although galaxies with central boxy regions represent the same structures viewed end-on ([Combes & Sanders 1981](#)), we do not consider these objects in our work.

The final sample of the galaxies with X-shaped structures comprises 151 objects in total. From our visual inspection, only a small part of the galaxies in the sample show no dust lanes. The X-structure may not be clearly seen due to the dust attenuation, and/or the orientation of the bar towards the observer, and/or a small angular size of the X-structure in a majority of the inspected objects.

The fact that only 7.5% out of the 2021 EGIS galaxies are selected as the galaxies with X-structures indicates that only the brightest, well-seen X-structures were identified.

While a prominent dust lane can signify whether a galaxy is viewed perfectly edge-on, it also severely affects derived structural parameters of edge-on galaxies. The influence of dust is significantly diminished when going from the optical SDSS bands to the near-infrared (NIR) domain. To study parameters of the X-structures in a NIR band, we added images of three galaxies (IC 2531, NGC 4013, and NGC 5529) observed at the  $3.6 \mu\text{m}$  with the *Spitzer* infrared telescope (IRAC, [Fazio et al. 2015](#)). IC 2531 does not fall into the SDSS DR12 footprint, whereas the other two galaxies do, but their discs and X-structures are severely distorted by the dust such that only small tips of their X-structures are visible above their dust lanes.

When we applied our method for determining the X-structure parameters (see Sect. 3) to the selected sample, we found out that for many galaxies the decomposition procedure (Sect. 3.2) does not converge to a robust model of the X-structure. There are several reasons for this. Perhaps, the most common issue is a small apparent size of the galaxy, and especially of the X-structure. Even if the X-structure is clearly detected by eye, it often covers too few pixels in the image to be fitted automatically. In many galaxies the X-structures are strongly obscured by the dust lane such that only their tips are visible. These X-structures are also easy to detect by eye but very difficult to process automatically, especially when the dust lane appears to be clumpy.

The final sample of galaxies for which our analysis was successful consists of 19 galaxies with the optical SDSS photometry, and of 3 more galaxies with available IRAC  $3.6\mu\text{m}$  observations. Thus, our sample cannot be considered as complete since it is likely biased towards bright massive galaxies, in which the most prominent X-structures are detected. We will refer to this sample of 22 galaxies as to the subsample.

<sup>1</sup> <http://www.sdss.org/dr12/>

**Table 1.** General parameters of the subsample galaxies with central X-structures

Name	$T$	$M_r$ mag	$g - r$ mag	$d_{25}$ arcmin	$z$
PGC 24926	2.0	-19.36	0.89	1.70	0.0054
PGC 26482	3.1	-20.66	0.90	1.17	0.0287
PGC 28788	0.5	-20.35	0.74	0.85	0.0178
PGC 28900	0.9	-21.55	0.81	1.00	0.0214
PGC 32668	0.0	-20.59	0.80	1.04	0.0215
PGC 37949	1.4	-20.82	0.93	1.32	0.0210
PGC 39251	-0.9	-20.73	0.73	1.69	0.0067
PGC 44422	0.4	-21.13	0.73	0.72*	0.0256
PGC 69401	1.0	-21.97	0.84	1.10	0.0312
PGC 34913	3.0	-20.89	0.90	1.91	0.0146
PGC 45214	1.0	-21.41	0.95	0.89	0.0406
PGC 10019	3.0	-20.96	0.82	0.78	0.0362
PGC 30221	3.0	-20.44	0.93	1.12	0.0209
PGC 55959	2.0	-21.38	0.91	1.02	0.0322
ASK 361026.0	4.6	-21.77	0.89	0.44*	0.0463
PGC 53812	3.9	-21.51	0.92	1.10	0.0359
PGC 02865	5.8	-20.01	0.86	1.78	0.0170
PGC 21357	3.3	-21.06	0.91	1.15	0.0393
PGC 69739	5.2	-20.92	0.94	2.00	0.0242
IC 2531	5.0	-22.49	–	6.60	0.0082
NGC 4013	3.1	-20.75	1.54	4.90	0.0027
NGC 5529	5.1	-22.23	0.85	5.75	0.0096

The columns show the name, morphological type, absolute magnitude in the SDSS  $r$  band, extinction-corrected colour ( $g-r$ ), and the diameter  $d_{25}$  from HyperLEDA. The last column shows the redshift from the NED database. \*: there is no diameter value in the HyperLEDA database, the values were taken from the NED database.

Table 1 summarizes some general properties of the subsample galaxies. The morphological type  $T$  and apparent diameter of the 25-th isophote in the  $B$ -band are taken from the HyperLEDA<sup>2</sup> database (Makarov et al. 2014). The redshift values are taken from the NED<sup>3</sup> database. We computed absolute magnitudes in the  $r$  band from our photometric models (see Sect. 3.2) using the luminosity distance and Galactic extinction values from the NED. The colours were computed from our models and corrected for the extinction in the Galaxy. Utilizing the decomposition models instead of the original images for the galaxy flux estimation allows one to exclude the contamination from background objects, and also solves the problem of the aperture size for performing the photometry: one can integrate an analytical model over a wide range of spatial coordinates to retrieve a precise value of the flux. The range of the integration was set to be 10 times the major axis of the 25-th isophote, to make sure that the total flux outside the integration boundaries is negligible.

The average values of the type and the absolute magnitude are  $\langle T \rangle = 2.3 \pm 1.8$ ,  $\langle M \rangle = -20.9 \pm 0.6$ , which suggests that our subsample consists of bright early-type spirals. The average observed colour of the galaxies ( $\langle g - r \rangle = +0.86 \pm 0.07$ ) is also consistent with edge-on early-type spirals (e.g., Bizyaev et al. 2014).

### 3 METHODS

In this section we describe the methods we used to extract parameters of the observed X-structures and their host galaxies. Our pipeline consists of three main steps: (i) preparation of galaxy images and generation of object masks, (ii) photometric decomposition of the final galaxy images, (iii) and subsequent measurement of the X-structure parameters.

#### 3.1 Images preparation

We retrieved images of the subsample galaxies in the  $r$  band data from SDSS DR12 (Eisenstein et al. 2011). Since some galaxies occupy more than one SDSS field (for example, if a galaxy is big enough or located close to the field edge) we used the SWARP package (Bertin et al. 2002) to concatenate adjacent fields.

The second step was to determine and subtract the sky background from the images. The SDSS pipeline includes a background subtraction routine, however we decided to perform our own background estimation to check for possible inaccuracies of the initial background subtraction. The algorithm of the background estimation was as follows. First, using the SEXTRACTOR code (Bertin & Arnouts 1996), we create a map of pixels which are not occupied by any object in the image. Then we fit the background intensity by a two-dimensional polynomial of the first order using only unmasked pixels. The weights of individual pixels in the fit are set to be the distance from the pixel to the nearest object. This allows us to minimize the influence of possible unmasked faint wings of extended objects.

After that, we rotated the images to align the galactic major axis along the  $x$ -axis. To estimate the position angle of the galaxy, we used the method described in Martin-Navarro et al. (2012). The main idea of the method is to measure the number of galaxy pixels which lie inside of a strip of a given width as a function of the position angle. The optimal value of the position angle is the one which gives the highest number of such pixels.

The next step was creating the point spread function (PSF) for every image of our subsample. Atmosphere blurring and telescope optics (to a less degree) can severely affect measured structural properties of galaxies (Trujillo et al. 2001). To compensate the effects of seeing during the decomposition process (see below), one has to take into account the PSF of the image. In this paper we adopt the Moffat (Moffat 1969) function as an analytical approximation to the observed PSF. To retrieve the parameters of the Moffat function, we selected several good (not crowded, bright, but not saturated) stars in the image and fitted them with the Moffat function. Then these fit parameters of individual stars were averaged to obtain robust values of the adopted PSF model.

The last step was creating the mask images to mask out background and foreground objects, the light of which can affect the observed properties of the galaxies. To create the mask images, we used catalogues of objects created with the SEXTRACTOR package (Bertin & Arnouts 1996) with subsequent manual inspection of the created masks.

The IRAC 3.6 $\mu$ m images of NGC 4013 and NGC 5529 were downloaded from the Spitzer Survey of Stellar Structure in Galaxies archive<sup>4</sup> (S4G, Sheth et al. 2010), along with the masks and weight (one-sigma) images. The sky background has already been

<sup>2</sup> <http://leda.univ-lyon1.fr/>

<sup>3</sup> NASA/IPAC Extragalactic Database, <https://ned.ipac.caltech.edu/>

<sup>4</sup> <http://irsa.ipac.caltech.edu/data/SPITZER/S4G/>

subtracted from these frames. For IC 2531 we used the observations available through the Spitzer Heritage Archive (the mosaic *\*maic.fits* and uncertainties *\*munc.fits* files from the post-Basic Calibrated Data). The sky background subtraction, rotation, cut out from the initial frames, and masking were carried out in a similar way as the SDSS frames. To obtain PSF kernels for these three galaxies, we used in-flight point response function (PRF) images for the centre of the IRAC 3.6 $\mu$ m field<sup>5</sup> downsampled to the 0.6 (IC 2531) or 0.75 (NGC 4013 and NGC 5529) arcsec/pixel scale and re-rotated to correspond to the analysed galaxy frame (the typical PSF FWHM for the IRAC 3.6 $\mu$ m images is 1.66 arcsec).

### 3.2 The Photometric Decomposition

The decomposition of a galaxy image is a widely used approach to obtain structural and photometric parameters of a galaxy. To perform the decomposition one has at first to construct a proper analytical model of the analyzed galaxy image and then find optimal parameters of this model via some optimisation procedure. The fit model should reflect the observed structure of the galaxy. It usually consists of separate components, which represent structural components of the galaxy. Below we describe the model which we adopt in this work and the algorithm to find optimal parameters of the model.

#### 3.2.1 The model

The main components of our model are a bulge, a disc, and an X-structure. The surface brightness distribution  $I(r)$  in the bulge is modeled with the Sérsic function (Sérsic 1968):

$$I(r) = I_e \exp \left( -\nu_n \left[ \left( \frac{r}{r_e} \right)^{1/n} - 1 \right] \right), \quad (1)$$

where  $I_e$  is the effective surface brightness,  $r_e$  — the effective radius,  $n$  — the Sérsic parameter, and  $\nu_n$  is a function depending on  $n$  (Caon, Capaccioli, D’Onofrio 1993).

The surface brightness of the disc in the “edge-on” orientation is usually represented by a two-dimensional function with the vertical and radial scale lengths. In the literature, one can find somewhat different approaches to represent this function. In this work we adopt it in the form consistent with that presented by Erwin (2015):

$$I(r, z) = 2hL_0 \frac{r}{h} K_1 \left( \frac{r}{h} \right) \operatorname{sech}^{2/m} \left( \frac{mz}{2z_0} \right), \quad (2)$$

where  $h$  is the radial scale length,  $z_0$  is the vertical scale height,  $K_1$  is the modified Bessel function, and  $L_0$  is the central luminosity density. The observed central surface brightness is related to  $L_0$  as  $I_0 = 2hL_0$ . The last parameter is  $m$ , which is often set to a constant value of 1, but in this work we set it as a free parameter of the model. Note, that with  $m \rightarrow \infty$  the vertical light distribution approaches the pure exponential shape (double exponential disc). Taking into account this fact, we set the upper limit on  $m$  to be 20.0 since the further increasing of this parameter does not affect the light distribution significantly: the difference between the disc with  $m = 20$  and the disc with a pure exponential vertical distribution is  $\sim 10^{-3}$  in terms of the total sum or residuals, therefore we can consider the discs with  $m = 20$  as ones with the exponential vertical profile.

To describe the observed surface brightness of an X-shaped structure, we use the modified Ferrers profile (Ferrers 1877):

$$I(r) = I_0 \left[ 1 - \left( \frac{r}{r_{\text{out}}} \right)^{2-\beta} \right]^\gamma, \quad r \leq r_{\text{out}}. \quad (3)$$

The Ferrers profile has four free parameters: the outer radius  $r_{\text{out}}$  and the central intensity  $I_0$ , along with two numerical values  $\beta$  and  $\gamma$ , which control the overall shape of the profile. The Ferrers profile has a central plateau with a steep decrease of the intensity in the outer regions, and it is often used to describe bars (see e.g. Laurikainen et al. 2007).

To add an X-shaped appearance to the Ferrers profile, we modulate it with the  $m = 4$  Fourier mode:

$$r = r_0 (1 + a_4 \cos(4(\phi + \phi_0))). \quad (4)$$

Here, the coefficient  $a_4$  regulates the strength of the X-shaped distortion, and  $\phi_0$  defines its overall rotation.

These three components described above (the disc, the bulge, and the X-structure) are present in every photometric model of each subsample galaxy. Although we strived to restrict the number of the model components, in some cases we had to introduce additional components (see below) when this simplified modelling was not satisfactory.

An important galaxy component is a dust structure, which is seen as a dimmed dust lane located close to the middle plane of the edge-on oriented galaxy. The simplest approach to account for the dust lane is to completely neglect it during the decomposition or to mask out the dust-reach region of the disc, however this can unpredictably affect the retrieved parameters of the decomposition. A more sophisticated and precise way is to add an additional dust component and run a radiative transfer code (see e.g. FITSKIRT, De Geyter et al. 2014) to create a self-consistent decomposition model, but this method is computationally consuming, especially for a sample of several dozens of objects. In this paper, we take the dust lane into account by adding it as a separate edge-on disc (2) with *negative* intensity (in other words, the dust model is being subtracted from the overall model of the galaxy in contrast with the other “regular” components). We added this dust component only for those galaxies where a dust lane was clearly seen.

Some galaxies in our subsample (for example, PGC 28900 and PGC 39251) demonstrate two blobs within the disc at both sides of the X-structure. These blobs are not rare in galaxies with X-shaped structures and arise in orbit simulations (Patsis, Skokos & Athanassoula 2002). In our model, we simulated the presence of such blobs by adding an edge-on oriented, three-dimensional ring with a Gaussian distribution of the luminosity density along the radial and vertical directions. This model component has four free parameters: the ring radius  $a$ , the luminosity density  $J_0$  at this radius and two Gaussian scales, radial and vertical. The observed two-dimensional brightness distribution is computed by the line-of-sight integration through the ring. When viewed edge-on, this model component appears as two bright areas on both sides from the centre.

In order to simplify the decomposition of galaxies with additional components (a dust lane or a ring), we split the whole procedure into two steps. The first step is to find a relatively simple “bulge+disc+X-structure” model. Then, in the second step, we add a ring or a dust lane component utilizing parameters of the simple model as initial conditions for the complex one.

We will refer hereafter to the galaxy model with all components except for the X-structure as a host model.

<sup>5</sup> <http://irsa.ipac.caltech.edu/data/SPITZER/docs/irac/calibrationfiles/>

All components of the model, along with their main described above parameters, have a set of additional parameters which determines their appearance in the image. These parameters are coordinates of the component centre  $x_c, y_c$ , ellipticity  $e$ , and position angle PA.

### 3.2.2 The decomposition procedure

The aim of the decomposition procedure is to find the best-fitting values of parameters of the multi-component model. These values can be found via optimisation algorithms, such as the Levenberg-Marquardt gradient descent algorithm (Levenberg 1944) or the Nelder-Mead simplex algorithm (Nelder, Mead 1965). The main issue here is to find proper initial parameters to pass them to optimisation iterations. If initial values are not close enough to their optimal values, the optimisation process can converge to one of possible local minima or even to singular points of the model function.

In this work we use the genetic algorithm (GA, Goldberg 1989) to find the initial conditions for gradient descent method. GA is a computational algorithm for searching solutions of an optimisation problem which simulates the natural selection process. The main idea of GA is to represent possible solutions of the problem as “organisms” with “genes” to be free parameters of a model. During the optimisation procedure these organisms evolve through the “breeding” and “mutation” processes to find a gene combination that minimises the fitted function:

$$f(g_1, g_2, \dots) = \sum_{i,j} w_{i,j} [I_{\text{obs}}(i, j) - I_{\text{model}}(i, j; g_1, g_2, \dots)]^2, \quad (5)$$

where  $I_{\text{obs}}(i, j)$  is the observed intensity at the pixel with the coordinates  $i$  and  $j$ ,  $I_{\text{model}}(i, j; g_1, g_2, \dots)$  is the model intensity depending on the particular set of genes, and  $w_{i,j} = \frac{1}{\sigma_{i,j}^2}$  are weights computed from per-pixel errors. The summation is performed over all unmasked image pixels. This function shows how close an organism to the solution of the problem is, and is called the fitness function.

The fitness function (5) is computed for a number of organisms (called a “generation”), and a subset of organisms is selected based on the best values of the fitness function. These organisms are used to create the next generation, and the cycling repeats until converging to optimal values. The iterations start with a zero generation which consists of organisms with randomly chosen parameter values.

In this work we set the generation size to be 250 organisms. The zero generation was twice as large. The iterations stop if the relative decrease of the generation-wide average value of the fitness function is less than  $10^{-6}$  for five generations in a row. To verify the quality of the obtained via GA solution, we use it as an initial guess to the gradient descent algorithm. We adopt the results of the gradient descent algorithm as the final decomposition parameters.

We use the flexible IMFIT package (Erwin 2015) as a basis for the decomposition engine. We modified its source code to include the X-shaped Ferrers function, and wrote a PYTHON<sup>6</sup> wrapper to parallelize computations for a large set of “genetic” populations.

Estimating uncertainties of the parameters retrieved by this decomposition procedure is a difficult task. The genetic algorithm

does not provide such estimates, and the gradient descent algorithm, which is used in the IMFIT package, provides only the lower limits of their values via the covariance matrix (Erwin 2015). One way to find the parameters uncertainties is to run the entire decomposition process several times. Since the startup procedure of the genetic algorithm includes a random zero generation, every run can converge to a slightly different model. One can use the scatter of the parameters obtained in every rerun, to estimate the corresponding confidence intervals.

Unfortunately, this approach is computationally expensive, therefore we decided to apply it to just one galaxy of our sample, in order to obtain typical values of uncertainties of the model parameters. We run the decomposition procedure 50 times for PGC 24926 and retrieved the following relative standard deviations of the parameters:  $\delta(\mu_e) = 13\%$ ,  $\delta(r_e) = 17\%$ ,  $\delta(n) = 11\%$ ,  $\delta(\mu_0) = 19\%$ ,  $\delta(h) = 2\%$ ,  $\delta(m) = 74\%$ ,  $\delta(z_0) = 4\%$  (only structural parameters given in Table 2 are listed). One can see that the highest uncertainty is for the parameter which governs the vertical shape of the disc,  $m$ . This can be caused by the dust attenuation and/or insufficient resolution of the vertical structure of this galaxy to reliably fit this parameter.

### 3.3 The X-structure analysis

The last step in the galaxy analysis is deriving parameters of its X-structure. To reduce the influence of the other galactic components (the disc, the bulge, etc.) on the measured properties of the X-structure, we subtract their models obtained during the decomposition from the original galaxy image. The residual image represents the X-structure.

After that, for each ray of the X-structure we make a set of photometric slices perpendicular to the ray direction and fit them with a Gaussian function in order to find the location of the maximum intensity points on the ray. Then we trace their location with a straight line, to obtain the mean direction of the ray. In the last step, we derive the length of the ray ( $l$ ) as a distance between the galaxy centre and the point along the ray where its intensity becomes fainter than  $I_b + 3\sigma_b$ , where  $I_b$  and  $\sigma_b$  are the background intensity and its uncertainty, respectively (this threshold roughly corresponds to the surface brightness level of 24 mag arcsec<sup>-2</sup> in the  $r$  band). Fig. 1 demonstrates a result of our analysis for PGC 32668. Another parameter, which we obtain from this analysis, is the angle  $\alpha$  between the ray and the galactic midplane.

Since the X-structure has four such rays, we performed this analysis for every ray separately and set the final parameters of the X-structure to be the mean values among all four rays.

Using the length of the obtained X-structure rays has a significant advantage in the comparison with utilizing the parameters of the Ferrers function. The Ferrers function does not contain any characteristic scale length, such as  $r_e$  for the Sérsic profile and  $h$  for the exponential disc. The parameter  $r_{\text{out}}$  shows where the surface brightness becomes exactly zero, but since the overall shape of the light curve is governed by the two power-law values  $\beta$  and  $\gamma$ , it is not evident where it goes through a given intensity level. Also, it is not defined how to compare the sizes of the Ferrers components with different  $\beta$  and  $\gamma$ . On the other hand, the length of an X-structure ray measured in photometric profiles has a straightforward meaning: the length is measured down to a given intensity level along the ray. We should stress here that the Ferrers component in our model, which describes the X-structure, is added to perform more reliable overall photometric decomposition of the galaxy. Using this approach, we are able to better fit the major struc-

<sup>6</sup> <https://www.python.org>

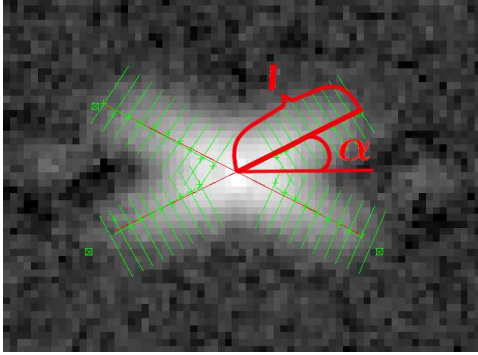


**Figure 1.** An example of the X-structure analysis. The thin lines perpendicular to the X-structure rays represent photometric cuts. The “+” sign on each slice shows the maximum location along the slice. The long thick lines show the linear fit to these points. The x-in-a-box signs indicate the limits of the fitting (see text). The estimated parameters  $l$  and  $\alpha$  are shown in the image for one ray.

tural components of the galaxy and, at the same time, to better trace the X-structure, defined as the residual between the galaxy image and the major model components.

## 4 RESULTS

### 4.1 The galactic environment

Before going to the decomposition analysis, we need to investigate the spatial environment of the galaxies with the X-structures. For this purpose, for the 151 galaxies in our total sample we estimate the number of neighbour galaxies using the SDSS DR12 database (Eisenstein et al. 2011).

We define a galaxy as a neighbour if it satisfies a set of requirements on its apparent angular distance from the target galaxy, the difference of their magnitudes, and radial velocities. To obtain more robust results, two different sets of such requirements were used:

- (i)  $\Delta r < 15r_{\text{petro}}$ ,  $\Delta m < 2\text{mag}$ ,  $|\Delta v| < 300\text{ km/s}$ ,
- (ii)  $\Delta r < 30r_{\text{petro}}$ ,  $\Delta m < 2.5\text{ mag}$ ,  $|\Delta v| < 300\text{ km/s}$ ,

where  $r_{\text{petro}}$  is the  $r$  band Petrosian radius of a target galaxy and  $\Delta v$  is the difference of radial velocities. The values of  $r_{\text{petro}}$  and  $m$  are taken in the  $r$  band. We will call these two sets of parameters for searching for neighbour galaxies as test 1 and test 2 sets.

Since the SDSS spectroscopic database is limited to  $m_r \approx 18\text{ mag}$  (Strauss et al. 2002), we need to restrict our samples to the magnitude  $m_r = 16\text{ mag}$  for the first set of parameters, and  $m_r = 15.5\text{ mag}$  for the second one, otherwise the limiting magnitude for the neighbours search will exceed 18 mag and the search will be performed in an incomplete domain of SDSS. After this restriction, our sample of galaxies with X-structures was reduced to 117 objects for the test 1 and 92 objects for the test 2.

The results of the described spatial environment test can be affected by some parameters of the galaxies: their apparent magnitudes and redshifts (due to incompleteness of the spectroscopic data for the faint end of the sample), and angular sizes (since the search range depends on them). In order to take these issues into account, the comparison sample should contain galaxies with similar distributions of these parameters.

The creation of the comparison sample was as follows. At

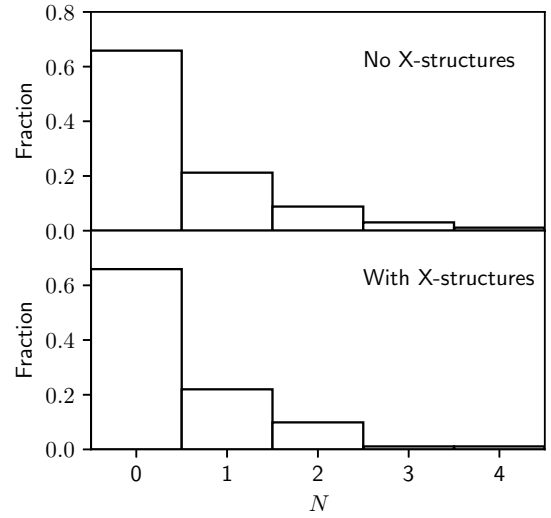


**Figure 2.** The distribution of the galaxies by the number of neighbours for the comparison sample (top) and our sample of galaxies with X-structures (bottom) according to the test 2 conditions (see text).

the first step we selected all edge-on galaxies from the Galaxy Zoo (Lintott et al. 2008) using the following restrictions on votes:  $P_{\text{EDGE}} > 0.95$ ,  $P_{\text{EL}} < 0.05$ ,  $P_{\text{CW}} < 0.05$  and  $P_{\text{ACW}} < 0.05$ , which means that only objects with high probability of being edge-on galaxy and low probability of being elliptical or non edge-on disc galaxy were selected. Then, for every galaxy in our main sample with X-structures we found all edge-on galaxies with similar size ( $\Delta R_{\text{petro}} < 20\%$ ), magnitude ( $\Delta m_r < 0.2\text{ mag}$ ) and redshift ( $\Delta z < 0.01$ ). Next, we checked images of all these similar galaxies visually and removed those that demonstrate signs of being X-shaped or show boxy central isophotes.

After this step, for every galaxy with the X-structure from our sample, we have got a set of galaxies with similar parameters, but without apparent X-shaped structures. To finally form the comparison sample, we randomly picked up one galaxy from every set. As a result, we obtained the comparison sample with similar distributions by angular size, apparent magnitude, and redshift and with the same size as our sample of galaxies with the X-structures.

Fig. 2 shows the distribution of galaxies of our sample and the comparison sample by the number of neighbours according to the test 2 conditions. The average number of neighbour galaxies for our sample is  $0.24 \pm 0.05$  for the test 1 set and  $0.54 \pm 0.10$  for the test 2 set (the standard errors of the mean are shown here). Corresponding values for the comparison samples are  $0.19 \pm 0.05$  and  $0.72 \pm 0.14$ . For both tests, the difference between the main number of neighbours lies within  $2\sigma$  limit, so we cannot consider this difference as statistically significant. We also used the two-sample Kolmogorov-Smirnov test to check if the distributions of galaxies by the number of neighbours are statistically different. The  $p$ -value (the probability of the null hypothesis) is 0.90 and 0.99 for the test 1 and the test 2 respectively, which means that these distributions are statistically indistinguishable.

This result is in agreement with Shaw (1987), where the analysis based on a sample of 23 galaxies with X-structures did not reveal a tendency of such galaxies to be located in a denser environment.

## 4.2 The decomposition of galaxies

Fig. 3 demonstrates results of the decomposition for three galaxies: PGC 69401, PGC 53812, and PGC 28788. The top panels show original images of the galaxies in the  $r$  band, the middle ones are the obtained models, and the bottom ones are the residuals (i.e., “image–model”). We applied three different models for these three galaxies. Our basic model consists of a disc, a bulge, and an X-structure (PGC 69401). The model of PGC 53812 contains the dust lane as an additional component, while the model of PGC 28788 also includes an edge-on ring (which can be seen as two bright blobs on both sides of the X-structure).

Below we provide results of the decomposition of galaxies from our subsample. We start with description of host galaxies (i.e., we list the parameters of main photometric components: the disc and the bulge) and then proceed with the parameters of the X-structure.

### 4.2.1 Host galaxies

Table 2 shows main structural parameters of the host galaxies: the effective surface brightness  $\mu_e$ , the effective radius  $r_e$ , the Sérsic index  $n$  of the bulge; and the central surface brightness  $\mu_0$ , the radial  $h$  and vertical  $z_0$  scales, and the vertical shape of the light curve  $m$  of the disc. The values are given for the  $r$  band for galaxies taken from SDSS and for the IRAC  $3.6\mu\text{m}$  band for galaxies with available *Spitzer* observations (three bottom lines in the table); the absolute magnitudes, along with  $\mu_e$  and  $\mu_0$  values, are corrected for the foreground Galaxy extinction according to the NED database (Schlafly & Finkbeiner 2011).

The last column in Table 2 shows the type of additional components (a ring or a dust lane) which were used in the decomposition model. One can see that for most galaxies either a dust component or a ring was added. Moreover, almost all galaxies that do not have a prominent dust lane, contain a ring component. This feature can be common in galaxies with X-structures. In many cases the rings may be obscured by dust.

We should emphasize that the values provided in Table 2 may be distorted by the dust lane attenuation because all galaxies are observed at the edge-on orientation where the dust influence is severe. This is especially significant for the bulges, which are seen entirely inside of the dust lane. However, our main goal of this decomposition is to separate the host galaxy light from the light of the X-structure, such that it can be analysed independently.

The mean value of the exponential scale in our subsample is  $\langle h \rangle = 3.9 \pm 1.3$  kpc (only galaxies from SDSS are taken into account). This means that the galaxies in our sample are comparable to or larger than the Milky Way (the exponential scale lengths of the Milky Way are  $3.00 \pm 0.22$  and  $3.29 \pm 0.56$  kpc for the thin and thick disks respectively according to MacMillan 2011).

### 4.2.2 The X-structures

Fig. 4 shows central regions of the images after subtracting from them the obtained models for the host galaxies. Different kinds of the X-structure shapes are clearly distinguishable: almost box-like in PGC 45214, with straight “rays” in PGC 28788 and PGC 32668, and the infinity sign-shaped in PGC 28900. One can also notice different axis ratios of the X-structures.

In the last two columns of Table 2 we list the parameters of the X-structures: the mean length of the rays  $l$  measured in kpc and normalised by  $h$  (values in brackets), and the mean angle  $\alpha$

between the rays and the disc midplane. Fig. 5 demonstrates the distributions of the  $\alpha$  and  $l$  in the X-structures. The average values of these parameters are  $\langle \alpha \rangle = (26.1 \pm 5.1)^\circ$  and  $\langle l \rangle = (1.18 \pm 0.50)h$ .

Since the most favoured scenario of the X-structure formation includes a bar, we decided to compare the observed distribution of the sizes of the X-structures for galaxies of our subsample with the distribution of bar sizes for galaxies viewed at a non edge-on orientation (i.e. for galaxies whose bars can be directly observed). We took observed bar sizes from Gadotti (2009), where the decomposition results of  $\sim 1000$  SDSS galaxies are provided. The mean exponential scale of barred galaxies from this sample is  $3.20 \pm 1.25$  kpc, which is similar to the mean value of our sample  $3.95 \pm 1.30$  kpc.

Fig. 6 shows the comparison of the X-structure semi-major axis size distribution (in projection on the galactic midplane) and the distribution of the bar sizes, both scaled to the disc exponential scale. One can see that the length of the semi-major axis for the most extended bars is approximately  $2.5h$ , therefore, one should not expect the X-structures to be larger than that. Indeed, The semi-major axis of all X-structures in our sample lies below this value. Moreover, the size of the X-structures is systematically smaller than the size of the bars: the maximum of the distribution of the X-structure sizes lies just above 1 kpc, whereas the distribution of the bar sizes reaches its maximum at about 1.7 kpc. This result is consistent with previous conclusions by Erwin & Debattista (2013), Herrera-Endoqui et al. (2015), and Erwin & Debattista (2017), who found that the spatial extent of the X-structures is about 0.38–0.54 of the bar length in moderately inclined galaxies.

Fig. 7 shows the relationship between the observed size of the X-structures and their vertical-to-lateral axis ratio. One can see that bigger X-structures have smaller axis ratios, in general. This can be easily explained within the bar-driven scenario. The observed length of the X-structure depends on the orientation of the bar with respect to the line of sight: the length is the largest when the bar is oriented perpendicular to the line of sight and gradually decreases if the bar is rotated toward the end-on orientation. On the other hand, the observed height of the X-structure should remain the same regardless of the bar orientation (as long as the observer stays within the disc midplane). Therefore, the observed height-to-length ratio varies with changing of the bar viewing angle.

### 4.2.3 The case of NGC 4013 and NGC 5529

As was mentioned above, two galaxies in our subsample, NGC 4013 and NGC 5529, have both SDSS and *Spitzer* images.

The dust lanes in these galaxies are extremely prominent and our approximate method of taking dust into account by adding a new dust component failed to fit a model. Instead, we started with decomposition in the IRAC  $3.6\mu\text{m}$  band where the dust influence is relatively small. Then we masked out dusty regions in the optical images and used the IR model as a starting point for the decomposition in the optical bands. The relatively wide PSF of the  $3.6\mu\text{m}$  image did not allow us to resolve a bulge for NGC 4013 and, therefore, the decomposition process converged to an unrealistic model with  $r_e = 0.1$  kpc.

Unfortunately, the inner parts of the X-structures in the optical bands are completely hidden by the dust lanes in these two galaxies. This circumstance did not allow us to perform the described above X-structure analysis and to obtain  $\alpha$  and  $l$  values in order to compare them with their IR counterparts. The only reliable pa-

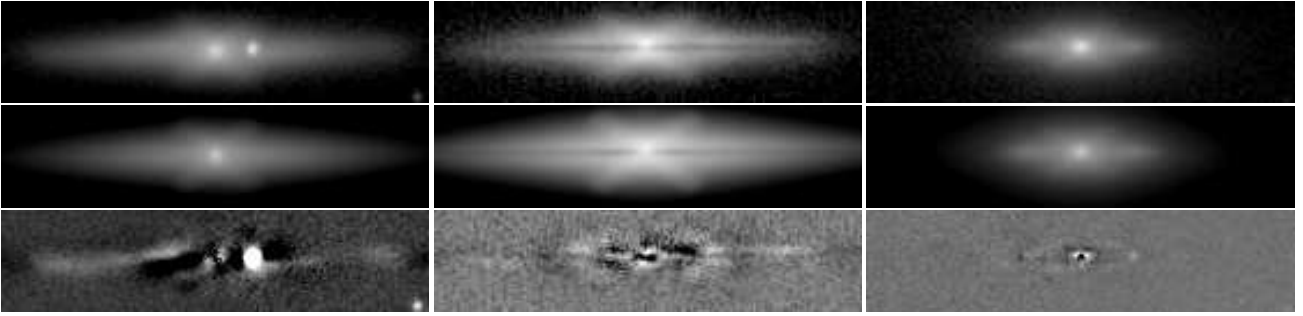


**Figure 3.** Results of the decomposition of three galaxies, left to right: PGC 69401, PGC 53812, PGC 28788. Top panels — the SDSS  $r$  band images, middle ones — models, bottom — residuals “image–model”. Three different models are shown: the most simple (bulge+disc+X-structure) for PGC 69401, with an additional dust lane for PGC 53812, and with an additional edge-on ring for PGC 28788.

Name	$\mu_e$ mag/□''	$r_e$ kpc	$n$	$\mu_0$ mag/□''	$h$ kpc	$m$	$z_0$ kpc	$l$ kpc ( $h$ )	$\alpha$ deg	add. comp.
PGC 24926	19.53	0.5	1.5	19.24	1.47	3.59	0.42	2.01 (1.37)	$21 \pm 3$	dust
PGC 26482	21.50	1.9	3.2	19.40	4.44	1.10	0.41	3.99 (0.90)	$28 \pm 2$	dust
PGC 28788	21.38	2.2	4.5	20.32	1.94	0.78	0.44	2.61 (1.35)	$26 \pm 1$	ring
PGC 28900	19.79	1.4	3.7	21.24	5.12	2.14	1.29	6.09 (1.19)	$22 \pm 1$	ring
PGC 32668	18.78	0.6	1.4	20.45	1.87	6.30	0.82	3.93 (2.10)	$29 \pm 0$	ring
PGC 37949	20.88	1.4	2.1	18.84	4.03	3.90	0.91	7.14 (1.77)	$28 \pm 4$	dust
PGC 39251	19.49	1.0	4.2	20.73	2.72	2.48	0.92	3.70 (1.36)	$15 \pm 2$	ring
PGC 44422	18.86	0.5	4.3	19.62	3.74	1.41	0.64	4.23 (1.13)	$23 \pm 2$	ring
PGC 69401	20.23	1.3	3.8	18.91	5.05	1.86	0.77	5.95 (1.18)	$27 \pm 3$	—
PGC 34913	21.44	1.3	2.5	18.74	4.34	20.00	0.66	3.56 (0.82)	$27 \pm 4$	dust
PGC 45214	19.81	1.5	0.7	17.93	3.72	12.91	0.59	7.74 (2.08)	$28 \pm 1$	dust
PGC 10019	20.62	2.1	1.2	18.37	3.65	6.18	0.54	5.88 (1.61)	$24 \pm 6$	dust
PGC 30221	20.87	1.6	1.6	19.08	3.09	2.98	0.47	4.32 (1.40)	$20 \pm 2$	dust
PGC 55959	21.05	1.9	2.3	18.41	3.94	20.00	0.25	6.02 (1.53)	$25 \pm 2$	dust+ring
ASK 361026.0	19.57	1.7	4.0	21.50	5.79	1.30	1.38	6.83 (1.18)	$22 \pm 2$	ring
PGC 53812	21.00	0.9	1.0	19.10	5.42	10.94	1.08	7.10 (1.31)	$26 \pm 1$	dust
PGC 02865	24.25	4.2	3.5	17.50	3.28	3.46	0.41	4.10 (1.25)	$32 \pm 1$	dust
PGC 21357	20.77	4.5	0.8	19.76	5.54	4.24	0.40	4.54 (0.82)	$35 \pm 3$	dust
PGC 69739	22.31	2.6	4.0	19.66	5.88	1.66	0.61	3.76 (0.64)	$27 \pm 1$	dust
IC 2531	21.11	1.2	4.7	24.07	8.25	20.00	0.62	2.81 (0.34)	$29 \pm 1$	—
NGC 4013	17.63	(0.1)	1.8	22.52	1.90	20.00	0.38	0.68 (0.36)	$22 \pm 1$	—
NGC 5529	21.79	1.2	3.3	22.84	8.00	20.00	0.25	2.00 (0.25)	$38 \pm 2$	—

**Table 2.** The structural parameters of the subsample galaxies: the effective surface brightness ( $\mu_e$ ), the effective radius ( $r_e$ ) and the Sérsic index ( $n$ ) of the bulge; the central surface brightness ( $\mu_0$ ), the radial exponential scale ( $h$ ), the  $m$ -value and the vertical scale ( $z_0$ ) of the disc; the mean length of X-structure rays ( $l$ ) and the mean angle between rays and the disc plane ( $\alpha$ ). All values are estimated in the  $r$  band. The last column shows the additional components of the model. The three bottom rows contain characteristics of the galaxies observed with the *Spitzer* telescope.

parameter that can be compared is the ellipticity  $e = 1 - b/a$  of the X-structure obtained from the photometric model. This parameter has close values for the optical ( $r$  band) and IR images: 0.32 and 0.28 for NGC 4013, 0.34 and 0.34 for NGC 5529.

## 5 N-BODY MODELLING

### 5.1 Simulations

In order to interpret the results of our photometric decomposition, we perform a set of  $N$ -body simulations and use snapshots of obtained models as input data to the procedure that we applied to the subsample of real galaxies. In our study we adopted a fiducial  $N$ -body model of the Milky Way which has been considered by MacMillan & Dehnen (2007).

The initial conditions of our simulation comprise three components: the disc, the bulge, and the dark halo. All three are live, i.e. described self-consistently, in order to allow exchange of angular momentum and, thus, a full bar growth (Athanasoula 2002, 2003).

The initial disc has an exponential surface density profile with a vertical structure modeled with isothermal sheets

$$\rho_d(r, z) = \frac{M_d}{4\pi h^2 z_0} \exp(-r/h) \operatorname{sech}^2\left(\frac{z}{z_0}\right), \quad (6)$$

where  $R$  is the cylindrical radius,  $h$  is the disc radial scale length,  $z_0$  is the disc scaleheight, and  $M_d$  is the total disc mass.

The dark halo model is a truncated NFW halo (Navarro, Frenk & White 1996, 1997) with the initial



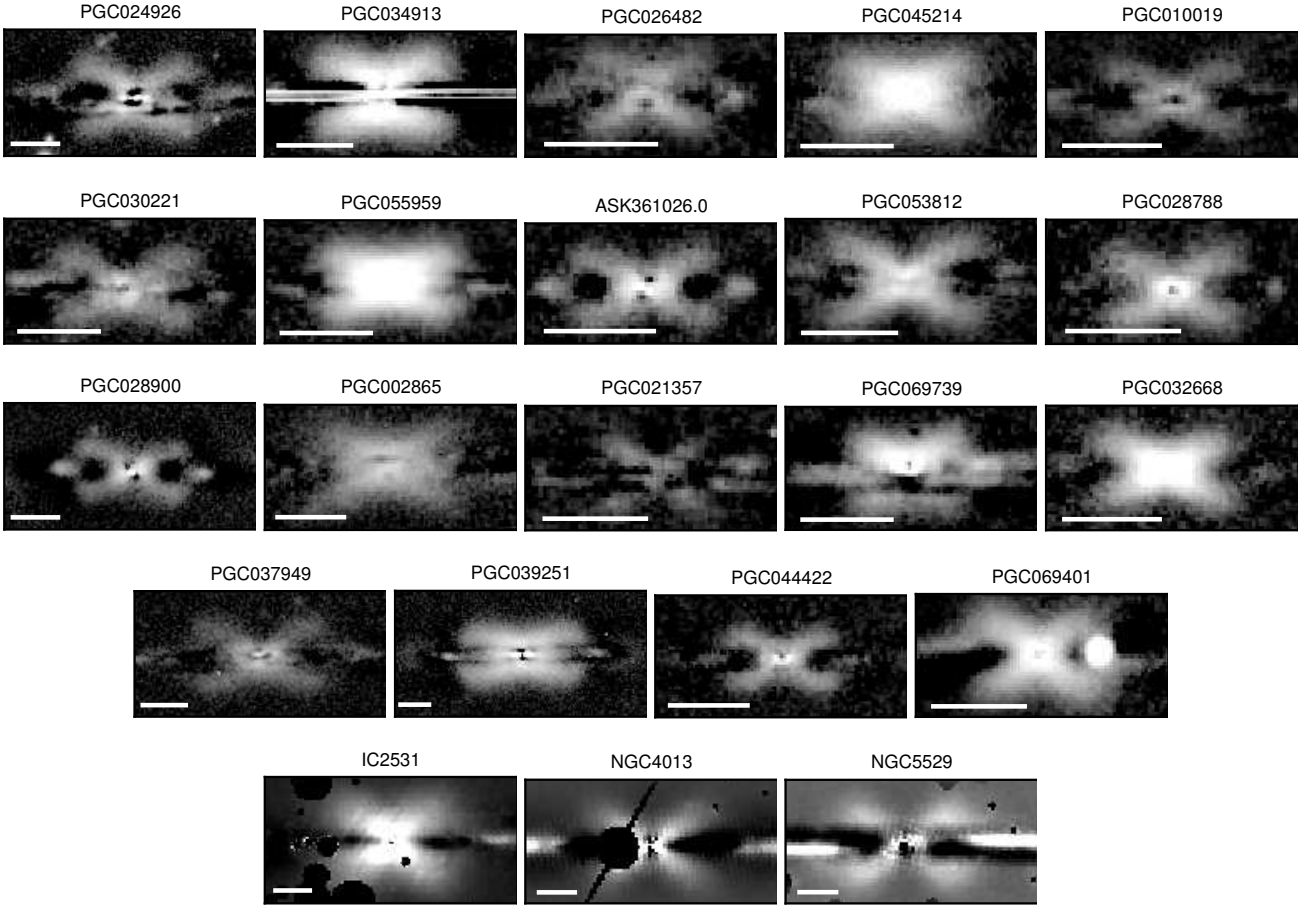


**Figure 4.** The central regions of the subsample galaxies after the host galaxy subtraction. The central X-structures are clearly visible. IRAC  $3.6\mu\text{m}$  images for the three galaxies are shown in the bottom row. The white bars in the bottom left corner of each image show the  $10''$  scale. The dark features in the images are masked regions.

volume density

$$\rho_h(r) = \frac{C_h \cdot T(r/r_t)}{(r/r_h)(1+r/r_h)^2}, \quad (7)$$

with  $T(r/r_t) = 2/(\exp(r/r_t) + \exp(-r/r_t))$ , where  $r$  is the radius,  $r_h$  and  $r_t$  are the halo core and cut-off radii, respectively, and the constant  $C_h$  is a parameter defining the full mass of the halo  $M_h$ .

The bulge is modeled with a [Hernquist \(1990\)](#) density profile

$$\rho_b(r) = \frac{M_b r_b}{2\pi r(r_b + r)^3}, \quad (8)$$

where  $r_b$  is a scale parameter and  $M_b$  is the total bulge mass.

We choose the units of these parameters such that the Newton's constant of gravity  $G = 1$ ,  $h = 1$ , and  $M_d = 1$ . We assume that the initial disc scale height is  $z_0 = 0.05$ , the bulge mass is  $M_b = 0.2$ , and scale length is  $r_b = 0.2$ . Scaling these values to the Milky Way disc, taking  $h = 3.5$  kpc and  $M_d = 5 \times 10^{10} M_\odot$ , gives the time unit of  $\simeq 14$  Myr, and the velocity unit of  $\sim 250 \text{ km s}^{-1}$ .

For the halo we take the scale radius as in [MacMillan & Dehnen \(2007\)](#)  $r_h = 6$ , the truncation radius  $r_t = 60$ , and the mass  $M_h = 24$ . Within a sphere of radius  $r = 4h$  the ratio  $M_h(4h)/M_d = 1.56$ .

In our tests the halo has 1 200 000 particles, the bulge – 40 000 and the disc – 200 000.

The initial conditions are built using the script `mkgalaxy` ([MacMillan & Dehnen 2007](#)) from the package `NEMO` ([Teuben 1995](#)). In the first step, the spherical initial conditions for the halo and the bulge in the presence of the monopole part of the disc potential as external potential are generated. Then both spheroids are adjusted to the presence of the full disc potential, rather than to only its monopole. The final step is to populate the disc component. In this step the potential of the halo and bulge are considered as external. The smoothed, azimuthally averaged potential of these components is described by the potential expansion.

The model evolves from the initial conditions with a dynamically cold disc, such that the Toomre parameter ([Toomre 1964](#))  $Q = 1.2$  at radius  $R = 2h$ . To simulate the evolution of the models, we use the fast  $N$ -body code `gyrfalcon` ([Dehnen 2000, 2002](#)). The gravitational softening lengths are  $\epsilon = 0.02$  for the disc and bulge particles, and 0.04 for halo particles. We vary the integration time step according to the rule  $0.1\sqrt{\epsilon/|\bar{a}|}$ , where  $\bar{a}$  is the gravitational acceleration. The opening angle was set to 0.6.

It has been long recognized that cool discs are unstable with respect to the bar-like instability (see a review by [Sellwood 2013](#)). In both cases we observe the formation of a bar after  $t = 50$ . The bar grows, and after  $t = 100$  it experiences the buckling instability

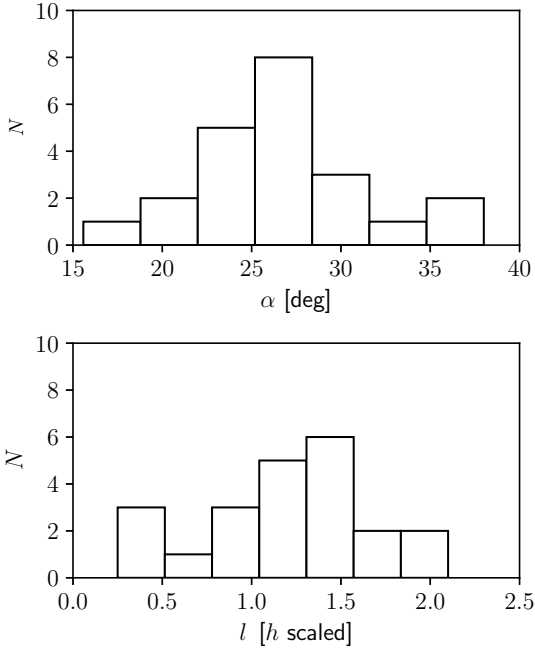


**Figure 5.** The distribution of the angle  $\alpha$  (top) and lengths normalized by  $h$  (bottom) of the X-structures.

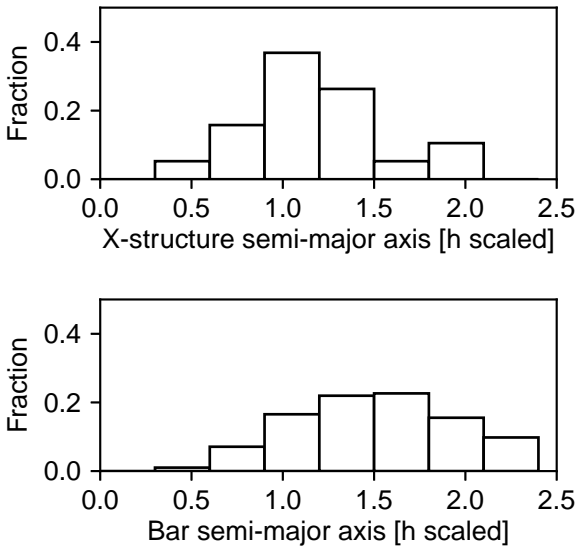


**Figure 6.** The size of the X-structures obtained in this work (top) versus the bar size from Gadotti (2009) (bottom). Values are normalised to the disk exponential scale-length.

that results in the formation of an X-structure. Fig.8 shows the disc at  $t = 200$ .

**5.2 The analysis of the  $N$ -body simulated images**

In this section we present results of the decomposition of our  $N$ -body model images described above. The big advantage of a  $N$ -body modelling approach is that we can control the orientation of

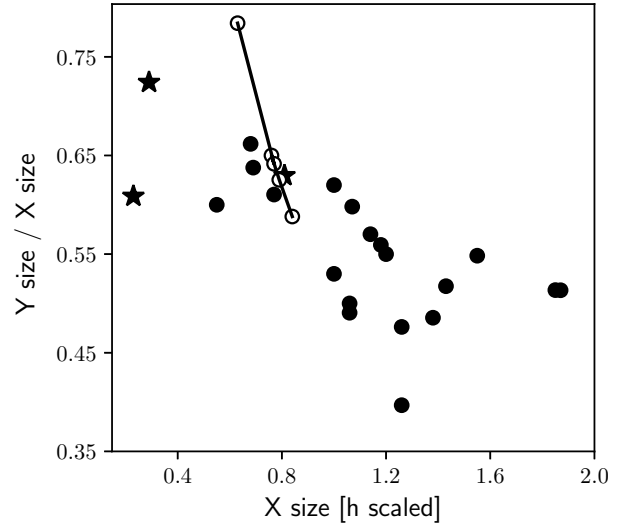


**Figure 7.** The relation between the X-structure semi-major axis size and its minor-to-major axis ratio. Circles — SDSS objects, stars — objects observed in the IRAC 3.6 $\mu$ m band. The open circles connected with the line represent the  $N$ -body simulations with different orientation (PA). (see Seq. 5.2).

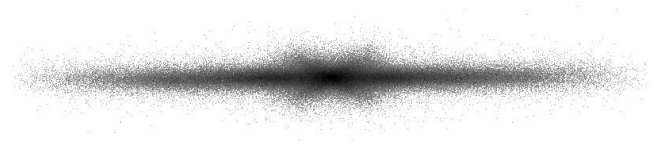


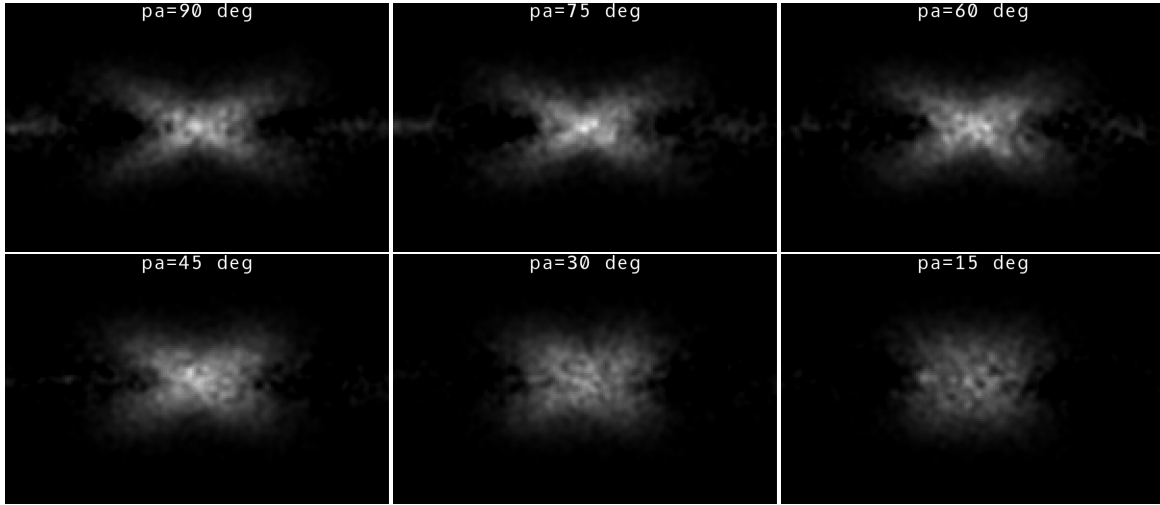
**Figure 8.** Log-scale density diagram of the edge-on view along the bar minor axis of the simulated disc. The presence of an X-shaped structure is clearly visible.

the galaxy and investigate how the observed parameters of the X-structure vary when we change the point of view.

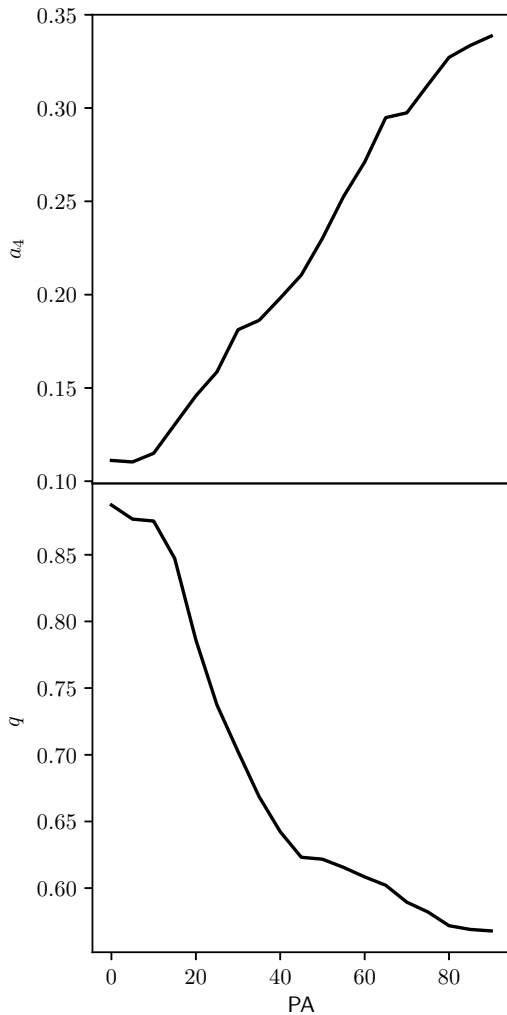
We performed the decomposition of simulated  $N$ -body model images generated for different points of view. We took  $N$ -body snapshots for  $t = 200$  at different points of view and gridded them into a 2D dataset by binning the  $x-z$  coordinates of all particles to a regular rectangular grid, keeping in each cell the logarithm of the number of particles. Then we used the NEMO tools to convert the gridded image into the FITS-format. The prepared this way data we considered as ‘observables’ and analyzed them as described in Sect. 3.

Fig. 9 shows a set of  $N$ -body images after the subtraction of the host photometric model. These images represent the same snapshot of the  $N$ -body model ( $t = 200$ ) viewed from different angles: the bar position angle varies from  $90^\circ$  (the bar is perpendicular to the line of sight) and to  $15^\circ$  (the bar is almost parallel to the line of sight). One can clearly observe how appearance of the X-shaped structure gradually changes from a strong X-like shape to a boxy one with the rotation of the galaxy.

Fig. 10 demonstrates how the  $a_4$  Fourier mode and the X-structure axis ratio changes with the bar orientation. As expected, the Fourier mode grows gradually as the bar orientation goes toward the side-on orientation, while the axis ratio gradually decreases. We argue that the behaviour of the axis ratio, which is



**Figure 9.** The images of the  $N$ -body models after the subtraction of the host model for different viewing angles from  $90^\circ$  (the bar is perpendicular to the line of sight) to  $15^\circ$  (the bar is almost parallel to the line of sight). The model images were convolved with a Gaussian kernel with FWHM of 3 pixels.



**Figure 10.** The dependence of the  $a_4$  Fourier amplitude (top) and the axis ratio (bottom) of the X-structure as a function of the bar position angle.  $PA = 0^\circ$  is the orientation when the bar is parallel to the line of sight.

shown in the bottom panel of Fig. 10, is responsible for the relation shown in Fig. 7, and which we observe in the real galaxies of our subsample.

To show how the galaxy moves in Fig. 7 with changing its position angle, we measured the size of the  $N$ -body X-structure along the  $x$ - and  $y$ -axes for different orientations of the model and plotted these values, along with the data for the subsample galaxies (white circles). The rightmost point corresponds to the bar orientation perpendicular to the line of sight ( $0^\circ$ ), and each next point demonstrates the addition of 15 degrees, i.e., the leftmost point shows the  $60^\circ$  orientation. One can see how the galaxy moves to the left when the position angle increases. A high value of the minor-to-major axis ratio for the leftmost point, which lies considerably above the points for the subsample galaxies, can be explained by a high value of the position angle for this point: real galaxies viewed from this angle probably will not demonstrate a prominent X-structure.

To compare the observed size of the X-structure with the bar size, we gridded the face-on projection of our  $N$ -body snapshot. Then we made a contour representation of a 2D image map and defined the distance along the major axis of a bar where the ellipticity of isodensities drops abruptly to zero. This distance estimates the extension of a bar  $1.75h$ . The procedure is similar to that described by Athanassoula & Misiriotis (2002). The size of the X-structure is about a half of the bar size. This result is in agreement with previous findings.

Another result we notice is the difference between the axis ratio in the real and simulated galaxies. The axis ratio in the models spans roughly from 0.6 to 0.8 for different orientations, whereas the axis ratio in the real galaxies can be as low as 0.4. Our model does not explain the existence of very flattened X-structures with the axis ratio less than  $\sim 0.6$ . Perhaps, such flattened structures may form in galaxies with more massive dark haloes, but it is a subject of a further investigation.

## 6 CONCLUSIONS

In this work we consider a sample of galaxies with prominent X-shaped structures at their centres. We develop a procedure for estimating the geometric parameters of the X-structures along with the parameters of their host galaxies. The procedure is applied to the

subsample of galaxies. In order to interpret the obtained results, we perform  $N$ -body simulations of a Milky Way-like galaxy and apply the same decomposition procedure to the simulated images.

Our main results are as follows:

- (i) galaxies with the X-structures reside in approximately the same local spatial environment as galaxies without such features;
- (ii) we estimate the structural parameters of the X-structures;
- (iii) the distribution of the X-structures by its apparent size shows a maximum at about 1.1 disc exponential scale lengths which is in agreement with previous findings drawn by other authors for face-on galaxies.
- (iv) There is a relation between the observed size of the X-structure and its axis ratio, which can be explained by the projection effect when a bar is viewed from different position angles.
- (v) We applied our decomposition procedure to the images created via the  $N$ -body modelling. The results for them are in qualitative agreement with those for the real galaxies.

Our main results confirm the bar-driven scenario of the X-structure origin. Although the analysis of our  $N$ -body simulations is in agreement with the results for the subsample galaxies, the characteristics of the X-structure for some galaxies significantly differ from the simulated ones. This requires a further investigation on a set of realistic  $N$ -body models with different input parameters, including the shape and the mass of the dark halo.

Another direction of a further development of this work is to apply our approach to a wider sample of galaxies. Application of our methods to the subsample, based on the optical SDSS images, showed that obscured by dust central regions of a galaxy is a big issue. A possible solution is to use edge-on galaxies with prominent X-structures from the S4G<sup>7</sup> catalogue (Sheth et al. 2010). The fact that we have successfully applied our procedure to the NIR images of the three galaxies, for which it failed in optics, shows that it is possible to apply our method for a larger sample of objects.

## ACKNOWLEDGEMENTS

We thank the anonymous reviewer for a thorough review and highly appreciate the comments and suggestions, which allowed us to significantly improve the quality of the publication.

Aleksandr Mosenkov is a beneficiary of a postdoctoral grant from the Belgian Federal Science Policy Office. Aleksandr Mosenkov also acknowledges support from St. Petersburg University research grant 6.38.335.2015.

DB acknowledges support from RSF grant RSCF-14-50-00043.

Funding for the Sloan Digital Sky Survey IV has been provided by the Alfred P. Sloan Foundation, the U.S. Department of Energy Office of Science, and the Participating Institutions. SDSS-IV acknowledges support and resources from the Center for High-Performance Computing at the University of Utah. The SDSS web site is [www.sdss.org](http://www.sdss.org).

SDSS-IV is managed by the Astrophysical Research Consortium for the Participating Institutions of the SDSS Collaboration including the Brazilian Participation Group, the Carnegie Institution for Science, Carnegie Mellon University, the Chilean Participation Group, the French Participation Group, Harvard-Smithsonian Center for Astrophysics, Instituto de Astrofísica de Canarias, The

Johns Hopkins University, Kavli Institute for the Physics and Mathematics of the Universe (IPMU) / University of Tokyo, Lawrence Berkeley National Laboratory, Leibniz Institut für Astrophysik Potsdam (AIP), Max-Planck-Institut für Astronomie (MPIA Heidelberg), Max-Planck-Institut für Astrophysik (MPA Garching), Max-Planck-Institut für Extraterrestrische Physik (MPE), National Astronomical Observatory of China, New Mexico State University, New York University, University of Notre Dame, Observatório Nacional / MCTI, The Ohio State University, Pennsylvania State University, Shanghai Astronomical Observatory, United Kingdom Participation Group, Universidad Nacional Autónoma de México, University of Arizona, University of Colorado Boulder, University of Oxford, University of Portsmouth, University of Utah, University of Virginia, University of Washington, University of Wisconsin, Vanderbilt University, and Yale University.

## REFERENCES

- Athanassoula E., 2002, *ApJ*, 569, 83  
 Athanassoula E., Misiriotis A., 2002, *MNRAS*, 330, 35  
 Athanassoula E., 2003, *MNRAS*, 341, 1179  
 Bertin E., Arnouts S., 1996, *A&AS*, 317, 393  
 Bertin E., Mellier Y., Radovich M. et al., 2002, *Astronomical Data Analysis Software and Systems XI*, 281, 228  
 Bizyaev D. V. et al., 2014, *ApJ*, 787, 24  
 Burbidge E. M., Burbidge G. R., 1959, *ApJ*, 130, 20  
 Bureau M., Freeman K. C., 1999, *AJ*, 118, 126  
 Bureau M., Aronica, G., Athanassoula, E., et al. 2006, *MNRAS*, 370, 753  
 Caon N., Capaccioli M., D’Onofrio M., 1993, *MNRAS*, 265, 1013  
 Ciambur B. C., Graham A. W., 2016, *A&A*, 96, 164  
 Ciambur B. C., Graham A. W., 2016, *MNRAS*, 459, 1276  
 Chung A., Bureau M., 2004, *AJ*, 127, 3192  
 Combes F., Sanders R. H., 1983, *A&A*, 96, 164  
 Combes F., Debbasch F., Friedli D., and Pfenniger D., 1990, *A&A*, 223, 82  
 De Geyter, G., Baes, M., Camps, P., Fritz, J., De Looze, I., Hughes, T. M., Viaene, S., Gentile, G. 2014, *MNRAS*, 441, 869  
 Dehnen W., 2000, *ApJ*, 536, 39  
 Dehnen W., 2002, *Journal of Computational Physics*, 179, 27  
 Eisenstein D. J. et al., 2011, *AJ*, 142, 72  
 Erwin P., 2015, *ApJ*, 799, 226  
 Erwin P., Debattista V. P., 2013, *MNRAS*, 431, 3060  
 Erwin P., Debattista V. P., 2017, *MNRAS*, 468, 2058  
 Freeman, K. C. 1970, *ApJ*, 160, 811  
 Fazio G. G. et al., 2004, *ApJS*, 154, 10  
 Ferrers N. M., 1877, *Quart. J. Pure Appl. Math.*, 14, 1  
 Gadotti D. A., 2009, *MNRAS*, 393, 1531  
 Goldberg D. E., 1989, *Genetic Algorithms in Search, Optimisation and Machine Learning* (Reading, MA: Addison-Wesley)  
 Hernquist L., 1990, *ApJ*, 356, 359  
 Herrera-Endoqui M., Díaz-García, S., Laurikainen E., Salo H., 2015, *A&A*, 582, A86  
 Herrera-Endoqui M., Salo H., Laurikainen E., Knapen J. H., 2017, *A&A*, 599, 23  
 Laurikainen E., Salo H., Buta R., Knapen J. H., 2007, *MNRAS*, 381, 401  
 Laurikainen E., Salo H., Buta R., Knapen J. H., 2011, *MNRAS*, 418, 1452  
 Laurikainen E., Salo H., Athanassoula E., Bosma A., Herrera-Endoqui M., 2014, *MNRAS*, 444, L80  
 Laurikainen E., Salo H., 2016, in ‘Galactic Bulges’, *Astrophysics and Space Science Library*, Volume 418. ISBN 978-3-319-19377-9. Springer International Publishing Switzerland, 2016, p. 77, E.Laurikainen, R.F.Peletier, D.A.Gadotti, publ. Springer  
 Laurikainen E., Salo H., 2017, *A&A*, 598, A10  
 Levenberg K., 1944, *Quarterly of Applied Mathematics*, 2, 164  
 Lintott C. J., Schawinski K., Slosar A., et al., 2008, *MNRAS*, 389, 1179  
 Lütticke R., Dettmar R.-J., Pohlen M., 2000, *A&AS*, 145, 405

<sup>7</sup> <http://irsa.ipac.caltech.edu/data/SPITZER/S4G/>

- MacMillan P.J., 2011, MNRAS, 414, 2446  
MacMillan P.J., Dehnen W., 2007, MNRAS, 378, 541  
Makarov D., Prugniel P., Terekhova N., Courtois H., & Vauglin I. 2014, A&A, 570, A13  
Martin-Navarro I., et al., 2012, MNRAS, 427, 1102  
Martinez-Valpuesta I., Shlosman I., Heller C., 2006, ApJ, 637, 214  
Méndez-Abreu J., et al, 2008, ApJ, 679, L73  
Moffat A. F. J., 1969, A&A, 3, 455  
Nataf D. M., Udalski A., Skowron J., Szymański M. K., Kubiak M., Pietrzyński G., Soszyński I., Ulaczyk K., Wyrzykowski Ł., Poleski R., Athanassoula E., Ness M., Shen J., and Li Z.-Y., 2014, MNRAS, 447, 1535  
Navarro J.F., Frenk C.S., White S.D.M., 1996, ApJ, 462, 553  
Navarro J.F., Frenk C.S., White S.D.M., 1997, ApJ, 490, 493  
Nelder J. A., Mead R., 1965, Computer Journal, 7, 308  
Ness M., Lang D., 2016, preprint (arXiv:1603.00026)  
Patsis P. A., Skokos Ch., Athanassoula E., 2002, MNRAS, 337, 578  
Pfenniger D., Friedli D., 1991, A&A, 252, 75  
Salo H., Laurikainen E., 2017, ApJ, 835, 252  
Sellwood, J. A. 2013, in *Planets Stars and Stellar Systems*, v. 5, eds. T. Oswalt & G. Gilmore (Heidelberg: Springer), 923  
Sérsic L. J., 1968, Atlas de Galaxias Australes, Observatorio Astronomico, Cordoba  
Shaw M. A., 1987, MNRAS, 229, 691  
Sheth, K., Regan, M., Hinz, J. L., et al. 2010, PASP, 122, 1397  
Schlafly E.F., Finkbeiner D.P., 2011, ApJ, 737, 103  
Strauss M.A., Weinberg D.H., Lupton R.H., 2002, AJ, 124, 1810  
Teuben P., 1995, ASP Conference Series, 77, 398  
Toomre A., 1964, ApJ, 139, 1217  
Trujillo I., et al., 2001, MNRAS, 328, 977  
Williams M.,J., et al., 2011, MNRAS, 414, 2163  
Yoshino A, Yamauchi C., 2015, MNRAS, 446, 3749

This paper has been typeset from a  $\text{\TeX/L\AA\TeX}$  file prepared by the author.